

---

# RadarOcc: Robust 3D Occupancy Prediction with 4D Imaging Radar

---

Fangqiang Ding<sup>1,\*</sup> Xiangyu Wen<sup>1,\*</sup> Yunzhou Zhu<sup>1</sup> Yiming Li<sup>2</sup> Chris Xiaoxuan Lu<sup>3</sup>

<sup>1</sup>University of Edinburgh <sup>2</sup>NVIDIA <sup>3</sup>UCL

## Abstract

3D occupancy-based perception pipeline has significantly advanced autonomous driving by capturing detailed scene descriptions and demonstrating strong generalizability across various object categories and shapes. Current methods predominantly rely on LiDAR or camera inputs for 3D occupancy prediction. These methods are susceptible to adverse weather conditions, limiting the all-weather deployment of self-driving cars. To improve perception robustness, we leverage the recent advances in automotive radars and introduce a novel approach that utilizes 4D imaging radar sensors for 3D occupancy prediction. Our method, RadarOcc, circumvents the limitations of sparse radar point clouds by directly processing the 4D radar tensor, thus preserving essential scene details. RadarOcc innovatively addresses the challenges associated with the voluminous and noisy 4D radar data by employing Doppler bins descriptors, sidelobe-aware spatial sparsification, and range-wise self-attention mechanisms. To minimize the interpolation errors associated with direct coordinate transformations, we also devise a spherical-based feature encoding followed by spherical-to-Cartesian feature aggregation. We benchmark various baseline methods based on distinct modalities on the public K-Radar dataset. The results demonstrate RadarOcc’s state-of-the-art performance in radar-based 3D occupancy prediction and promising results even when compared with LiDAR- or camera-based methods. Additionally, we present qualitative evidence of the superior performance of 4D radar in adverse weather conditions and explore the impact of key pipeline components through ablation studies.

## 1 Introduction

The safety of autonomous vehicles navigating in the wild hinges on a thorough understanding of the environment’s 3D structure. As a unified scene representation built from grid-based volumetric elements known as voxels, 3D occupancy has gained increasing attention within the autonomous driving community [1–5]. Its rising popularity stems from its comprehensive scene depiction, capturing both geometric and semantic aspects. Crucially, it transcends the limitations of foreground-only representations (vs. 3D object detection [6–8]) and sparse data formats (vs. point cloud segmentation [9–11]). Furthermore, 3D occupancy offers a detailed open-set depiction of scene geometry, effectively handling out-of-vocabulary items (e.g., animals) and irregular shapes (e.g., cranes). This capability allows it to address a broader range of corner cases than previous object-based perception approaches [12–14].

Previous research has predominantly utilized either LiDAR point clouds [2, 15–22], RGB images [4, 5, 23–33], or a combination of both [3] for 3D occupancy prediction. However, the potential of 4D imaging radar—a critical sensor in autonomous driving—has been largely untapped in this area. Evolving from traditional 3D mmWave radars, this emerging sensor type enhances elevation

---

\*Equal contribution

resolution, enabling detection and resolution of targets across both horizontal and vertical planes, which results in detailed *imaging* outputs. Meanwhile, 4D radar inherits the traditional advantages of mmWave radar, such as capability in all lighting and weather conditions, object velocity measurement, and cost-effectiveness compared to LiDAR systems. These attributes, particularly its resilience in adverse weather conditions like fog and rain, position 4D radar as an essential component in achieving mobile autonomy.

In this work, we explore the potential of 4D imaging radar to enhance 3D occupancy prediction. Previous research in radar perception has largely relied on 4D radar point clouds as input, a method inspired by LiDAR techniques. This ‘LiDAR-inspired’ framework has demonstrated effectiveness in tasks such as 3D object detection and tracking [34–56]. However, this approach primarily enhances the detection of foreground objects such as cars, pedestrians, and trucks. In contrast, 3D occupancy prediction requires the detection of signal reflections from all occupied spaces, encompassing both foreground and background elements like roads, barriers, and buildings. The traditional reliance on sparse radar point clouds, therefore, is not optimal for 3D occupancy prediction, as critical environmental signals are often lost during the point cloud generation process [57, 58]. For instance, the surface of highways, typically made of low-reflectivity materials such as asphalt, often yields weak signals back to the radar receiver.

To avoid the loss of negligible signal returns, we propose utilizing the 4D radar tensor (4DRT) for 3D occupancy prediction. This raw data format preserves the entirety of radar measurements, offering a comprehensive dataset for analysis. However, employing such volumetric data introduces significant challenges. For instance, the substantial size of 4DRTs—potentially up to 500MB—poses processing inefficiencies that could compromise real-time neural network performance. Additionally, raw radar data is inherently noisy due to the multi-path effect and is stored in spherical coordinates, which diverges from the preferred 3D Cartesian occupancy grid used in our applications.

Motivated by the outlined challenges, we introduce a novel approach, RadarOcc, specifically tailored for 4DRT-based 3D occupancy prediction. To address the computational and memory demands, our method initially reduces the data volume of 4DRTs through the encoding of Doppler bins descriptors and implementing spatial sparsification in the preprocessing stages. Our technique features sidelobe-aware spatial sparsification to minimize the interference scattered across azimuth and elevation axes, which is further refined through range-wise self-attention mechanisms. Importantly, we observed the typical conversion of spherical RTs to Cartesian data volumes, which often incurs non-negligible interpolation errors. Instead, we directly encode spatial features in spherical coordinates and seamlessly aggregate them using learnable voxel queries defined in Cartesian coordinates. Our approach further employs 3D sparse convolutions and deformable attention [59] for efficient feature encoding and aggregation. RadarOcc is benchmarked on the K-Radar dataset [40] against state-of-the-art methods across various modalities, demonstrating the promising performance in radar-based 3D occupancy prediction. Comprehensive experiment results validate its comparable performance to the camera and LiDAR solutions. A qualitative assessment further validates the superior robustness of 4D radar data under adverse weather conditions, establishing its capability for all-weather 3D occupancy prediction. The contributions of this work are three-fold:

- Introduction of the first-of-its-kind method, RadarOcc, for 4D radar-based 3D occupancy prediction in autonomous driving. We recognize the limitation of radar point clouds in reserving critical raw signals and advocate the usage of 4DRT for occupancy perception.
- Development of a novel pipeline with techniques to cope with challenges accompanying 4DRTs, including reducing large data volume, mitigating sidelobes measurements and interpolation-free feature encoding and aggregation.
- Extensive experiments on the K-Radar dataset, benchmarking state-of-the-art methods based on different modalities, and validating the competitive performance of RadarOcc and its robustness against adverse weather. Our code will be made public upon acceptance.

## 2 Related work

**3D occupancy prediction.** Early attempts on 3D occupancy prediction, *aka.* semantic scene completion (SSC) [60], are mainly limited to the small-scale interior scenes [60–69]. The introduction of SemanticKITTI [70] expands the study of SSC to large-scale outdoor scenes, based on which some works validate the feasibility of outdoor SSC with LiDAR input [15–19]. In contrast, MonoScene [23] is the seminal work for SCC using only a single monocular RGB image. Since Tesla’s disclosure of

their occupancy network for Full Self-Driving (FSD) [1], there has been a recent surge of research on 3D occupancy prediction for autonomous vehicles. While a few works leverage LiDAR point clouds [2, 3, 20–22] for scene completion, the majority of existing approaches rely on a vision-only pipeline that learns to lift 2D features into the 3D space [3–5, 24–33]. Despite these prevalent solutions based on LiDAR and camera, 4D radar sensors are still under-explored for 3D occupancy prediction.

**4D radar for autonomous driving.** As an emerging automotive sensor, 4D mmWave radar prevails over LiDAR and camera in adverse weather (*e.g.*, fog, rain and snow), offering all-weather sensing capabilities for mobile autonomy. In recent years, increasing endeavours have been witnessed to unveil the potential of 4D radar for autonomous driving applications, encompassing 3D object detection [34–55] and tracking [54–56], scene flow estimation [71, 72], odometry [71, 73–79] and mapping [77–79]. Apart from these works, we are the pioneering study for 4D radar-based 3D occupancy prediction, further exploring this unique sensor for the untouched topic.

**Radar tensor for perception** Besides the post-processing radar point cloud, another data type of mmWave radar is the radar tensor (RT), which is the product of applying FFT along the corresponding dimensions to the raw ADC samples (*c.f.* Sec. 3.1). Unlike the sparse radar point cloud, dense RTs contain rich and complete measurements of the environment, refraining from information loss during point cloud generation (*e.g.*, CFAR [57, 58]). Consequently, some works attempt to use 2D [35, 80–83], 3D [84–86] or 4D [40, 44, 50] RTs for object detection, yielding satisfactory performance. In this work, we develop a tailored approach to 4D radar-based 3D occupancy prediction based on 4DRTs.

### 3 Preliminary

#### 3.1 4D radar signal processing pipeline

**ADC samples.** To measure the surroundings, a sequence of FMCW waveforms, aka. chirp signals, are emitted by the transmit (Tx) antennas within a short timeframe. These signals are reflected off objects and captured by the receive (Rx) antennas. The intermediate frequency (IF) signal is produced by mixing the signals from a Tx-Rx antenna pair. This mixed signal is then sampled by an Analog-to-Digital Converter (ADC) to generate discrete samples for each chirp [87]. By compiling ADC samples from all chirps and Tx-Rx antenna pairs, the FMCW radar system constructs a 3D complex data cube for each frame. This data cube is organized into three dimensions: *fast time*, *slow time*, and *channel*, which correspond to range, range rate, and angle, respectively [88].

**Radar tensor.** Utilizing ADC samples, Fast Fourier Transforms (FFTs) are applied across relevant dimensions to extract detailed information. The first FFT, known as range-FFT, is performed across the sample (fast time) axis to separate objects at different distances into distinct frequency responses within range bins defined by hardware specifications. Subsequently, a Doppler-FFT along the chirp (slow time) axis decodes phase variances—Doppler bins—to derive relative radial velocities, producing a range-Doppler heatmap. For configurations with multiple Rx-Tx antenna pairs, termed *virtual antenna elements*, additional FFTs (angle-FFT) are executed across the spatial dimensions of the virtual antenna array to determine Angles of Arrival (AoA) for azimuth and elevation angles. This series of transformations results in a comprehensive 4D radar tensor (4DRT), characterized by power measurements across range, Doppler velocity, azimuth, and elevation dimensions.

**Radar point cloud.** Beyond analyzing radar tensors, most FMCW radar sensors further refine their output to identify salient targets, which typically represent less than 1% of the data. Target detection algorithms such as CA-CFAR [57] and OS-CFAR [89] are commonly applied to the range-doppler heatmap [88, 90] or directly on the 3D/4D radar tensors [40, 44] to isolate peak measurements. This process generates a sparse radar point cloud, with each point characterized by 3D coordinates and attributes such as Doppler velocity, power intensity, or radar cross-section (RCS). While this step significantly reduces data volume and mitigates noise, it also eliminates a substantial amount of potentially valuable information.

#### 3.2 4DRT for 3D occupancy prediction

**Rationale of using 4DRT.** 4D radar tensors (4DRTs) serve as raw sensor data that amalgamate the strengths of LiDAR/radar point clouds and RGB images, providing direct 3D measurements in a continuous data format. These tensors comprehensively capture information from raw radar measurements, effectively addressing the shortcomings associated with the sparseness of radar point

clouds caused by the signal post-processing. For instance, low-reflectivity surfaces like asphalt, common on highways, typically do not reflect enough radar signals for detection. By using 4DRTs, these minimal signal returns can be detected, significantly bolstering occupancy prediction capabilities. Furthermore, the volumetric structure of 4DRTs aligns well with 3D occupancy grids, making them ideally suited for advancing 3D occupancy prediction techniques.

**Challenges.** Despite their significant advantages, using 4D radar tensors (4DRTs) for 3D occupancy prediction presents substantial challenges. First, the large data size of 4DRTs (e.g., 500MB per frame in the K-Radar dataset [40]) hinders computational efficiency, necessitating data volume reduction before processing. Second, the inherent noise in radar data, exacerbated by the multi-path effect of mmWave, requires careful filtering to preserve essential signals while eliminating noise. Third, the discrepancy between the spherical coordinates of 4DRT data and the Cartesian coordinates required for 3D occupancy outputs calls for a tailored network design. This design must effectively translate spatial interactions from spherical to Cartesian dimensions to ensure accurate occupancy predictions.

## 4 Method

### 4.1 Task definition

In this work, we consider the task of 3D occupancy prediction with single-frame 4DRT output from 4D imaging radar. Given a 4DRT captured in the current frame denoted as  $\mathbf{V} \in \mathbb{R}^{R \times A \times E \times D}$ , our task aims to predict a 3D volume  $\mathbf{O} = \{o_i\}_{i=1}^{H \times W \times L}$ , of which each voxel element  $o_i \in \{c_0, c_1, \dots, c_C\}$  is represented as either free (*i.e.*,  $c_0$ ) or occupied with a certain semantics  $c_i (i > 0)$  out of  $C$  classes. Here,  $R$ ,  $A$ ,  $E$ , and  $D$  denote the number of bins along the range, azimuth, elevation and Doppler axis, respectively, and each scalar of the 4DRT is the power measurement mapped to a location within the space defined by these four axes.  $H$ ,  $W$  and  $L$  represent the volumetric size of the predefined region of interest (RoI) in the height, width and length dimensions.

### 4.2 Overview

RadarOcc consists of four components in tandem (*c.f.* Fig. 1). Before loading heavy 4DRTs to the neural network, we reduce their data volume as the preprocessing steps via encoding the Doppler bins descriptor and performing sidelobe-aware spatial sparsifying to improve the efficiency without losing the key information (*c.f.* Sec. 4.3). To refrain from the interpolation error, we encode spatial features directly on the spherical RTs without transforming them into Cartesian volumes (*c.f.* Sec. 4.4) and aggregate the spherical features with 3D volume queries defined in the Cartesian coordinates (*c.f.* Sec. 4.5). Specifically, range-wise self-attention is used to alleviate the sidelobes, and sparse convolution and deformable attention are leveraged for fast feature encoding and aggregation. The occupancy probabilities are predicted in the 3D occupancy decoding step, which is supervised via our training loss (*c.f.* Sec. 4.6).

### 4.3 Data volume reduction

Direct processing of raw 4DRTs with neural networks is impractical due to its substantial data size (*e.g.*, 500MB per frame) which leads to heavy computation cost and memory usage. Moreover, the slow data transfer between the sensor, storage device and processing unit (CPU/GPU) of large-volume raw 4DRTs not only hinders the onboard runtime efficiency but also increases the training duration which demands repetitive data loading. For efficiency, we propose to reduce the data volume of 4DRTs through encoding the Doppler bins descriptor and sidelobe-aware spatial sparsifying as the preprocessing steps (see Fig. 1). Post reduction, the loading of 4DRTs into the processing unit for runtime inference can be more feasible and the network training can be more efficient.

**Doppler bins descriptor.** Unlike the three spatial axes, which are intuitively critical for spatial perception, the Doppler axis in 4DRTs has often been considered redundant in 3D object detection. Previous studies [40, 44, 50] have employed average-pooling to minimize this axis, aiming to reduce computational overhead. However, we argue that this ostensibly ‘redundant’ axis contains vital cues for geometric and semantic analysis in 3D occupancy prediction. Specifically, the Doppler axis provides essential information on object speed via peak locations, aiding in differentiating dynamic objects from static backgrounds. Moreover, the power distribution within the Doppler bins offers

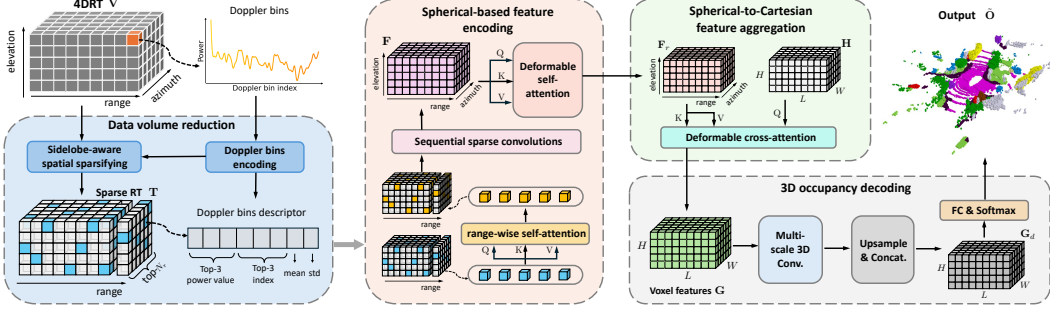


Figure 1: Overall pipeline of RadarOcc. The data volume reduction pre-processes the 4DRT into a lightweight sparse RT via Doppler bins encoding and sidelobe-aware spatial sparifying. We apply spherical-based feature encoding on the sparse RT and aggregate the spherical features using Cartesian voxel queries. The 3D occupancy volume is finally output via 3D occupancy decoding.

insights into the confidence levels of true targets—essentially, indicating their likelihood of occupancy. To preserve and utilize this crucial information, we have developed a method to encode the Doppler bins into a descriptor that captures specific statistics for each spatial location within the 4DRTs. This descriptor incorporates the top-three power values along with their indices, the mean power value, and the standard deviation, as depicted in Fig 1. Note that the number of preserved top values is determined empirically. Consequently, this approach enables us to reduce the data volume of raw 4DRTs by a factor of  $\frac{D}{8}$ , while retaining key information from the Doppler axis.

**Sidelobe-aware spatial sparsifying.** By encoding the Doppler bins into light-weight descriptors, we transform the raw 4DRT into 3D spatial data volume with the original Doppler axis as the 8-channel feature dimension. Nevertheless, it remains costly for neural networks to encode features from 3D dense data volume with operations like 3D convolution [91, 92]. To accelerate the computation, prior arts [40, 44] transfer the dense RT into a sparse format by retraining only the top-percentile elements based on power measurements. However, this approach tends to be biased towards specific ranges that exhibit exceptionally high measurements. It can be observed in Fig. 2 that after percentile-based sparsifying, a significant number of the reserved elements are concentrated within the same ranges spread across the azimuth and elevation axes. These elements manifest as artifacts of sidelobes, which can be viewed as the diffraction pattern of the antenna [93, 94]. Consequently, this results in the loss of important measurements from other ranges and introduces lots of noise into the sparse tensor. To mitigate this issue, we propose to select the top- $N_r$  elements for each individual range instead of on the whole dense RT for spatial sparsifying (see Fig. 1). In this way, the dominance of certain ranges can be avoided while the sidelobe level is reduced, as exhibited in Fig. 2. Note that our spatial element selection is based on the mean power value across the Doppler axis. The final sparse tensor is denoted as  $\mathbf{T} = \{t_i \in \mathbb{R}^{N_r \times (8+2)}\}_{i=1}^R$  with the extra two feature channels storing the azimuth and elevation indices of reserved  $N_r$  elements for each range.

#### 4.4 Spherical-based feature encoding

Given the sparse RT, we aim to encode representative features for accurate 3D occupancy prediction. As the sparse RTs are inherently in the spherical coordinates, previous works [40, 44] transfer them into the Cartesian coordinates before feature encoding. However, such a transfer would undermine their uniform density distribution and often incur interpolation errors. Inspired by the polar representation of point clouds [10, 95, 96], we propose to take the elements in RT as voxels rasterized in the spherical coordinates and apply the spherical-based feature encoding directly. The spherical voxel representation naturally matches the spherical-uniform distribution of RTs and can refrain from inducing interpolation errors. In practice, the 3D convolutions can be used to extract grid-based representations by only replacing the  $X$ - $Y$ - $Z$  axis with the range-azimuth-elevation axis. In what follows, we illustrate our spherical-based feature encoding process.

**Range-wise self-attention.** In Section 4.3, we address the issue of sidelobes by selecting elements based on range-wise percentiles during the preprocessing phase. To further mitigate sidelobe interference, we introduce a range-wise self-attention mechanism [97] (see Fig. 1) as the initial step in our feature encoding process. Specifically, within each range component  $t_i \in \mathbf{T}$ , which includes  $N_r$  RT



Figure 2: Comparison between the sparse RTs resulted by our sidelobe-aware and percentile-based sparsifying [40, 44]. We transform the spherical RT elements to the Cartesian coordinates and show them in two views. The arches on the heatmap indicate the same ranges. Percentile-based method retains many elements caused by sidelobe noise, which are concentrated at certain ranges. In contrast, our method can reduce the sidelobe level and reserve critical measurement from different ranges.

tokens, we utilize the Doppler bin descriptors as token features. Additionally, two index channels are employed for positional embeddings to enhance the specificity of our spatial encoding.

**Sequential sparse convolution.** For efficiency, we apply a series of 3D sparse convolutions [98] onto the sparse RT for spatial feature encoding in the spherical voxel space. This produces a 3D dense feature volume  $\mathbf{F} \in \mathbb{R}^{\frac{R}{S} \times \frac{A}{S} \times \frac{E}{S} \times C_f}$  ( $N_f = \frac{R}{S} \times \frac{A}{S} \times \frac{E}{S}$ ) with a reduce spatial dimension characterized by the stride  $S$ , where  $C_f$  denotes the feature dimension. Note that  $\mathbf{F}$  inherently aligns with the spherical space with each feature element’s indices corresponding to a spherical coordinate.

**Deformable self-attention.** Following the consecutive 3D sparse convolution, we use the 3D deformable attention [59] to further refine and augment our feature volume  $\mathbf{F}$  by enforcing spatial interaction. As a definition, for a query feature  $z$  corresponding to a reference point  $p$  in the input feature  $\mathbf{X}$ , its feature can be updated by deformable attention in the following equation:

$$\text{DeformAttn}(z, p, \mathbf{X}) = \sum_{m=1}^M \mathbf{W}_m \left[ \sum_{k=1}^K \mathbf{A}_{mk} \cdot \mathbf{W}'_m \mathbf{X}(p + \Delta p_{mk}) \right] \quad (1)$$

where  $\mathbf{W}_m$  and  $\mathbf{W}'_m$  are the learnable weights for the  $m$ -th attention head, while  $\mathbf{A}_{mk}$  and  $\Delta p_{mk}$  is the attention weight and sampling offset calculated with  $z$  for its  $k$ -th sampling point and the  $m$ -th head.  $\mathbf{X}(p + \Delta p_{mk})$  is the key features at the sample location  $(p + \Delta p_{mk})$ . By applying self-attention to  $\mathbf{F} = \{f^q\}_{q=1}^{N_f}$ , the refined feature volume  $\mathbf{F}_r = \{f_r^q\}_{q=1}^{N_f}$  can be derived by:

$$f_r^q = \text{DeformAttn}(f^q, p^q, \mathbf{F}) \quad (2)$$

#### 4.5 Spherical-to-Cartesian feature aggregation

Decoding 3D Cartesian occupancy from a spherical feature volume is inherently challenging due to misalignments in spatial axes and discrepancies in the regions they represent. An intuitive approach would be to transform the spherical feature volume into a Cartesian one and then decode the 3D Cartesian occupancy. However, this method can introduce feature-level interpolation errors, which we aim to avoid as discussed in Section 4.4.

To avoid conducting interpolation, we propose to aggregate the spherical features in a *learnable* way, with 3D volume queries defined in the Cartesian coordinates attending to the feature samples in  $\mathbf{F}_r$ , as shown in Fig. 1. First, we build learnable grid-based voxel queries  $\mathbf{H} = \{h^q \in \mathbb{R}^{C_f}\}_{q=1}^{H \times W \times L}$  which has the same volumetric size as our desired output  $\mathbf{O}$  and the same feature dimension as the spherical feature volume  $\mathbf{F}_r$ . Each voxel query  $h^q$  corresponds to a 3D point  $p^q$  in the Cartesian coordinate. Second, the 3D point  $p^q$  of each query is transformed from the Cartesian to the spherical coordinate, which is then mapped to a index position in  $\mathbf{F}_r$  denoted as  $\Phi(p^q)$ . We take  $\Phi(p^q)$  as a 3D reference point in the spherical space and sample key elements in its vicinity from the feature volume  $\mathbf{F}_r$ . Lastly, we leverage deformable cross-attention [59] to aggregate the key samples for each reference point and the output  $\mathbf{G} = \{g^q \in \mathbb{R}^{C_f}\}_{q=1}^{H \times W \times L}$  can be calculated by:

$$g^q = \text{DeformAttn}(h^q, \Phi(p^q), \mathbf{F}_r) \quad (3)$$

#### 4.6 3D occupancy decoding and supervision

With the aggregated voxel features  $\mathbf{G}$ , we leverage consecutive 3D convolutions [91, 92] with skip connection [99] to decode hierarchical feature volumes at  $N_s$  scales with a scaling step of 2. Multi-

scale feature volumes are then merged in a top-down way [100] via upsampling features by a factor 2 and concatenated along the feature dimension, resulting in  $\mathbf{G}_d \in \mathbb{R}^{H \times W \times L \times N_s C_f}$ . Finally, the occupancy head equipped with the *softmax* function is employed to output the normalized occupancy probabilities  $\tilde{\mathbf{O}} \in \{0, 1\}^{H \times W \times L \times (C+1)}$  for all voxels on  $C$  semantic classes and one free class.

Our network is trained in a supervised way with the ground truth occupancy. Following [3], we use the cross-entropy loss as the primary loss to optimize the training and incorporate the lovasz-softmax loss [101] to handle the class imbalances. Moreover, we utilize the scene- and class-wise affinity loss proposed in [23] to enhance the optimization of geometry and semantic IoU metrics.

## 5 Experiment

### 5.1 Experimental setup

**Dataset preparation.** Our experiments are conducted on the K-Radar dataset [40], which is, to the best of our knowledge, the only autonomous driving dataset providing available 4DRT data. Besides, K-Radar also contains multi-modal data from LiDAR, camera, GPS-RTK and annotated 3D bounding boxes and tracking IDs, enabling us to compare between different modalities and generate 3D occupancy labels. Following [3, 25, 102], we generate occupancy ground truth by superimposing consecutive LiDAR sweeps and construct the dense 3D occupancy grids via voxelization. To handle scene dynamics, we register objects with the same tracking IDs across the sequence. As K-Radar does not annotate fine-grained point-level semantics, we segment the scene into the foreground (*e.g.*, sedan, truck, pedestrian) and background using bounding boxes and label the voxel grids into three classes, including foreground, background and free. Many sequences in K-Radar were collected under adverse weather (*i.e.*, sleet, rain, and snow), which results in non-negligible noise to the generated occupancy labels based on LiDAR sweeps. Therefore, we reserve this adverse-weather test split for qualitative comparison and only generate the occupancy labels for the well-condition sequences, which are separated into the training, validation and test splits.

**Evaluation protocol.** As the pioneering study of 3D occupancy prediction using the K-Radar dataset, we have tailored the evaluation protocol to align with our experimental needs. We define the Region of Interest (RoI) with specific dimensions: a front range of [0, 51.2m], a side range of [-25.6m, 25.6m], and a height range of [-2.6m, 3m]. The voxel resolution is set at 0.4m, resulting in a target occupancy volume of  $128 \times 128 \times 14$  voxels. Consistent with established methods in the field [3, 70, 102], we employ the Intersection over Union (IoU) metric to evaluate the geometric accuracy of our occupancy predictions, focusing solely on the occupied or free status without integrating semantics. Additionally, to gauge the effectiveness of our foreground-background segmentation, we calculate the mean IoU (mIoU) across these two classes. In line with previous studies [5, 102], we present our findings across multiple ranges, specifically at 51.2m, 25.6m, and 12.8m.

**Competing methods.** We benchmark RadarOcc against state-of-the-art methods employing different modalities. Given that recent studies do not use radar data for 3D occupancy prediction, we adapt the OpenOccupancy LiDAR-based baseline and CONet [3] to accommodate radar point cloud (RPC) inputs for our comparative analysis. Furthermore, we convert 4DRTs to Cartesian coordinates [40] with a voxel size of 0.4m, referred to as 4DRT-XYZ, and integrate them into the LiDAR-based OpenOccupancy framework [3]. Following best practices from [40, 44], we process 4DRT-XYZ into a sparser format. For a comprehensive inter-modality evaluation, we also replicate the OpenOccupancy LiDAR-based baseline [3] and both monocular and stereo camera-based SurroundOcc [25] configurations to fit our experimental setup. Notably, we enrich our comparisons by generating 16-beam and 32-beam LiDAR point clouds from the standard 64-beam configurations through elevation-wise downsampling. The evaluation focuses on the overlap area between the horizontal field of view (FoV) of all sensors and our defined RoI to minimize potential data discrepancies beyond the FoV. For implementation, we train all evaluated models on our K-Radar well-condition training set.

### 5.2 Comparison against radar-based methods

We first compare RadarOcc with state-of-the-art baseline methods using radar data for 3D occupancy prediction in Tab. 1. As can be seen, RadarOcc outperforms other approaches in every metric, demonstrating its state-of-the-art performance in radar-based 3D occupancy prediction. Specifically, our 4DRT-based RadarOcc largely improves the performance over RPC-based methods: the mIoU of

Method	Input	IoU (%)			mIoU (%)			BG IoU (%)			FG IoU (%)		
		12.8m	25.6m	51.2m									
L-baseline [3]	RPC	42.8	34.9	27.9	23.5	18.6	14.6	43.5	34.6	27.3	3.5	2.6	1.9
L-CONet [3]	RPC	46.1	36.0	25.0	24.6	20.3	14.4	43.3	35.4	25.6	5.8	5.2	3.1
L-baseline [3]	4DRT-XYZ	47.4	38.1	28.5	29.9	24.3	17.5	46.4	37.5	27.9	13.4	11.1	7.2
RadarOcc (Ours)	4DRT	<b>48.8</b>	<b>39.1</b>	<b>30.4</b>	<b>34.3</b>	<b>28.5</b>	<b>22.6</b>	<b>47.9</b>	<b>38.2</b>	<b>29.4</b>	<b>20.7</b>	<b>18.7</b>	<b>15.8</b>

Table 1: Quantitative comparison between RadarOcc and state-of-the-art radar-based baseline methods. Results are reported on K-Radar well-condition test split. Best result is shown in **bold**.

Method		IoU (%)			mIoU (%)			BG IoU (%)			FG IoU (%)		
		12.8m	25.6m	51.2m									
(a)	Ours	<b>48.8</b>	39.1	<b>30.4</b>	<b>34.3</b>	28.5	<b>22.6</b>	<b>47.9</b>	38.2	<b>29.4</b>	<b>20.7</b>	18.7	15.8
(b)	Ours w/o DBD	48.1	<b>39.4</b>	30.0	33.6	<b>28.9</b>	22.6	47.2	<b>38.7</b>	29.2	20.0	<b>19.1</b>	<b>16.0</b>
(c)	Ours w/o SSS	44.2	36.8	28.7	24.1	20.2	15.6	42.3	35.6	27.6	5.9	4.7	3.5
(d)	Ours w/o SFE	46.2	38.4	29.4	30.4	26.5	21.1	45.5	37.5	28.5	15.4	15.5	13.9

Table 2: Ablation studies on key designs of RadarOcc. DBD, SSS, SFE refer to the Doppler bins descriptor, sidelobe-aware spatial sparsifying, and spherical-based feature encoding, respectively.

L-CONet [3] is relatively improved by 39.4%, 40.4% and 56.9% for different volumes (12.8m, 25.6m, 51.2m). Such a significant improvement mainly stems from the dense data format of 4DRT, which retains critical information from low-reflectivity objects, enabling effective occupancy prediction for the whole scene. 4DRT-XYZ based L-baseline [3] also outperforms RPC-based methods but inferior to RadarOcc, especially in long-range FG IoU. We credit this to the interpolation errors led to small and far foreground objects when we converting 4DRT to Cartesian coordinates.

### 5.3 Ablation study

To validate the effectiveness of our key designs, we ablate them alone from our 4DRT-based pipeline RadarOcc and show the evaluation results on K-Radar well-condition test split in Tab. 2.

**Doppler bins descriptor.** By replacing the Doppler bins descriptor with the average-pooling result, the performance of RadarOcc is degraded in most metrics (row (a) vs. (b) in Tab. 2), demonstrating the usefulness of preserving the information encoded by the Doppler axis (c.f. Sec. 4.3). However, the improvement is somehow marginal due to the limited Doppler measurement range of the radar used in K-Radar [40], which wraps around the overflow values, causing ambiguity in Doppler velocity.

**Sidelobe-aware spatial sparsifying.** We conduct this experiment (row (c) in Tab. 2) by changing our sidelobe-aware spatial sparsifying (c.f. Sec. 4.3) to the percentile-based spatial sparsifying used in [40, 44]. Our sidelobe-aware approach leads to a remarkable advancement in performance, especially in mIoU metrics. This is attributed to its ability to preserve more valid elements from diverse ranges and suppress sidelobes for sparse RTs, allowing for more accurate prediction.

**Spherical-based feature encoding.** For row (d) in Tab. 2, we transform sparse RT to Cartesian coordinates before feature encoding (c.f. Sec. 4.4) and omit the spherical-to-Cartesian feature aggregation (c.f. Sec. 4.5). We can see that our spherical-based feature encoding gains the performance for each metric as our strategy preserves the original data distribution, avoiding incurring interpolation errors. This also validates the effectiveness of our learnable spherical-to-Cartesian feature aggregation.

### 5.4 Comparison between different modalities

To enrich our benchmark results and provide insights into the performance comparison between different modalities, we also evaluate state-of-the-art baseline methods [3, 25] on LiDAR and camera input. Quantitative results on K-Radar well-condition test split are reported in Tab. 3, while examples of qualitative results on K-Radar adverse-weather testing splits are exhibited in Fig. 3.

**Quantitative results under normal weathers.** As seen in Tab. 3, not surprisingly, LiDAR-based L-baselines [3] rank the top three in most metrics thanks to LiDAR’s low-noise and high-resolution measurements (vs. radar) and direct depth measurement (vs. camera). Due to the inherently lower resolution and considerable noise of radar data, radar-based methods exhibit inferior to

Method	Input	IoU (%)			mIoU (%)			BG IoU (%)			FG IoU (%)		
		12.8m	25.6m	51.2m									
L-baseline [3]	L (16)	<b>49.1</b>	<b>43.3</b>	<b>35.2</b>	<b>39.0</b>	<b>34.3</b>	<b>28.2</b>	<b>48.2</b>	<b>42.5</b>	<b>34.4</b>	<b>29.8</b>	<b>26.1</b>	<b>22.1</b>
	L (32)	<b>51.1</b>	<b>44.0</b>	<b>34.9</b>	<b>42.1</b>	<b>35.0</b>	<b>28.9</b>	<b>50.8</b>	<b>43.6</b>	<b>34.2</b>	<b>33.5</b>	<b>26.3</b>	<b>23.6</b>
	L (64)	<b>56.9</b>	<b>52.5</b>	<b>43.8</b>	<b>53.7</b>	<b>45.2</b>	<b>36.6</b>	<b>56.1</b>	<b>51.8</b>	<b>43.3</b>	<b>51.2</b>	<b>36.5</b>	<b>29.9</b>
SurroundOcc [25]	C	44.3	33.1	24.1	36.1	23.9	14.7	44.1	32.9	23.7	28.2	15.0	5.7
	C (S)	46.2	34.4	25.4	<b>40.8</b>	25.4	16.2	45.5	34.1	25.1	<b>36.1</b>	16.7	7.3
RadarOcc (Ours)	4DRT	<b>48.8</b>	<b>39.1</b>	<b>30.4</b>	34.3	<b>28.5</b>	<b>22.6</b>	<b>47.9</b>	<b>38.2</b>	<b>29.4</b>	20.7	<b>18.7</b>	<b>15.8</b>

Table 3: Quantitative comparison between RadarOcc and state-of-the-art methods based on LiDAR and camera. Results are reported on K-Radar well-condition test split. (·) is the number of LiDAR beams and (S) denotes stereo. The top four methods are colored as **red**, **green**, **blue**, and **orange**.

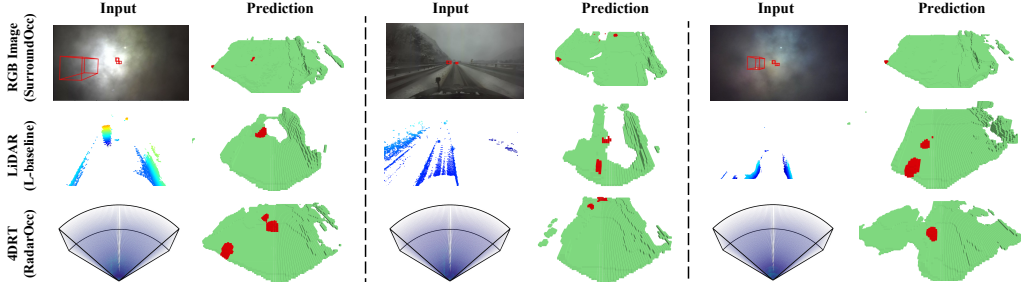


Figure 3: Qualitative comparison between RadarOcc, LiDAR-based L-baseline [3] and camera-based SurroundOcc [25] in adverse weathers. Ground truth bounding boxes are shown in RGB images.

LiDAR-based methods in normal weather. However, RadarOcc still shows comparable performance to 16-beam LiDAR, and surpasses monocular and stereo camera-based method in most metrics. Notably, RadarOcc outperforms state-of-the-art SurroundOcc [25] relatively by 39.5%/19.7% and 53.7%/26.1% in mIoU/IoU@51.2m for stereo and monocular input, respectively. Stereo camera-based SurroundOcc [25] ranks third on FG IoU and mIoU@12.8m because of stereo vision’s ability to infer accurate depth at short ranges, where the disparity between the two images is more pronounced.

**Qualitative results under adverse weathers.** While we have demonstrated the competitive performance of RadarOcc under normal weather, the key reason behind using radar for perception comes from its unique robustness against adverse weather where LiDAR and cameras fall short. To showcase such an inherent advantage, we provide some examples of qualitative results from different modalities in Fig. 3. As can be seen, RadarOcc provide robust 3D occupancy prediction under heavy rain and snow. In contrast, the camera lens are covered by the rain/snow and LiDAR measurements of some objects ahead are missing as water droplets or snowflakes can scatter and absorb the laser beams, leading to worse results. Please see our supplementary materials for more qualitative results.

## 6 Conclusion

In this work, we propose RadarOcc, a novel 3D occupancy prediction approach based on 4DRTs output from 4D imaging radar, enabling robust all-weather perception for autonomous vehicles. We analyse the rationale and challenges of using 4DRTs for 3D occupancy prediction and present tailored solutions to cope with the large, noisy and spherical 4DRTs. Experiments on the K-Radar dataset show RadarOcc’s state-of-the-art performance in radar-based 3D occupancy prediction and comparable results to other modalities in normal weathers. Through qualitative analysis, we also exhibit its unique robustness against various adverse weathers. We believe our work could endorse the potential of 4D imaging radar to be an alternative to LiDAR and setup an effective baseline for further research and development of 4D radar-based occupancy perception.

**Limitations.** As an initial investigation into 4D radar-based 3D occupancy prediction, this work has several limitations as follows. First, our method maps single-frame 4D radar data to single-frame 3D occupancy prediction without modeling the temporal information and performing occupancy forecasting. Second, due to the lack of point-wise annotation, our task is limited to two general semantics, *i.e.*, foreground and background. Future work will aim to address these issues.

## References

- [1] Tesla. Tesla AI Day 2022. [https://www.youtube.com/watch?v=0DSJsviD\\_SU](https://www.youtube.com/watch?v=0DSJsviD_SU), 2022. Accessed: 2024-04-08. 1, 3
- [2] Ben Agro, Quinlan Sykora, Sergio Casas, and Raquel Urtasun. Implicit occupancy flow fields for perception and prediction in self-driving. In *Proceedings of the IEEE/CVF Conference on Computer Vision and Pattern Recognition (CVPR)*, pages 1379–1388, 2023. 1, 3
- [3] Xiaofeng Wang, Zheng Zhu, Wenbo Xu, Yunpeng Zhang, Yi Wei, Xu Chi, Yun Ye, Dalong Du, Jiwen Lu, and Xingang Wang. Openoccupancy: A large scale benchmark for surrounding semantic occupancy perception. In *Proceedings of the IEEE/CVF International Conference on Computer Vision (ICCV)*, pages 17850–17859, 2023. 1, 3, 7, 8, 9
- [4] Xiaoyu Tian, Tao Jiang, Longfei Yun, Yucheng Mao, Huitong Yang, Yue Wang, Yilun Wang, and Hang Zhao. Occ3d: A large-scale 3d occupancy prediction benchmark for autonomous driving. *Advances in Neural Information Processing Systems*, 36, 2024. 1, 3
- [5] Yiming Li, Zhiding Yu, Christopher Choy, Chaowei Xiao, Jose M Alvarez, Sanja Fidler, Chen Feng, and Anima Anandkumar. Voxformer: Sparse voxel transformer for camera-based 3d semantic scene completion. In *Proceedings of the IEEE/CVF Conference on Computer Vision and Pattern Recognition (CVPR)*, pages 9087–9098, 2023. 1, 3, 7
- [6] Tingting Liang, Hongwei Xie, Kaicheng Yu, Zhongyu Xia, Zhiwei Lin, Yongtao Wang, Tao Tang, Bing Wang, and Zhi Tang. Bevfusion: A simple and robust lidar-camera fusion framework. *Advances in Neural Information Processing Systems*, 35:10421–10434, 2022. 1
- [7] Zhijian Liu, Haotian Tang, Alexander Amini, Xinyu Yang, Huizi Mao, Daniela L Rus, and Song Han. Bevfusion: Multi-task multi-sensor fusion with unified bird’s-eye view representation. In *Proceedings of the IEEE International Conference on Robotics and Automation (ICRA)*, pages 2774–2781. IEEE, 2023. 1
- [8] Xuanyao Chen, Tianyuan Zhang, Yue Wang, Yilun Wang, and Hang Zhao. Futr3d: A unified sensor fusion framework for 3d detection. In *Proceedings of the IEEE/CVF Conference on Computer Vision and Pattern Recognition (CVPR)*, pages 172–181, 2023. 1
- [9] Lingdong Kong, Youquan Liu, Runnan Chen, Yuxin Ma, Xinge Zhu, Yikang Li, Yuenan Hou, Yu Qiao, and Ziwei Liu. Rethinking range view representation for lidar segmentation. In *Proceedings of the IEEE/CVF International Conference on Computer Vision (ICCV)*, pages 228–240, 2023. 1
- [10] Qi Chen, Sourabh Vora, and Oscar Beijbom. Polarstream: Streaming object detection and segmentation with polar pillars. *Advances in Neural Information Processing Systems*, 34:26871–26883, 2021. 1, 5
- [11] Xin Lai, Jianhui Liu, Li Jiang, Liwei Wang, Hengshuang Zhao, Shu Liu, Xiaojuan Qi, and Jiaya Jia. Stratified transformer for 3d point cloud segmentation. In *Proceedings of the IEEE/CVF Conference on Computer Vision and Pattern Recognition (CVPR)*, pages 8500–8509, 2022. 1
- [12] Ming Liang, Bin Yang, Wenyuan Zeng, Yun Chen, Rui Hu, Sergio Casas, and Raquel Urtasun. Pnpnet: End-to-end perception and prediction with tracking in the loop. In *Proceedings of the IEEE/CVF Conference on Computer Vision and Pattern Recognition (CVPR)*, pages 11553–11562, 2020. 1
- [13] Junru Gu, Chenxu Hu, Tianyuan Zhang, Xuanyao Chen, Yilun Wang, Yue Wang, and Hang Zhao. Vip3d: End-to-end visual trajectory prediction via 3d agent queries. In *Proceedings of the IEEE/CVF Conference on Computer Vision and Pattern Recognition (CVPR)*, pages 5496–5506, 2023. 1
- [14] Yihan Hu, Jiazhi Yang, Li Chen, Keyu Li, Chonghao Sima, Xizhou Zhu, Siqi Chai, Senyao Du, Tianwei Lin, Wenhui Wang, et al. Planning-oriented autonomous driving. In *Proceedings of the IEEE/CVF Conference on Computer Vision and Pattern Recognition (CVPR)*, pages 17853–17862, 2023. 1
- [15] Ran Cheng, Christopher Agia, Yuan Ren, Xinhai Li, and Liu Bingbing. S3cnet: A sparse semantic scene completion network for lidar point clouds. In *Proceedings of the Conference on Robot Learning (CoRL)*, pages 2148–2161. PMLR, 2021. 1, 2

[16] Luis Roldao, Raoul de Charette, and Anne Verroust-Blondet. Lmscnet: Lightweight multiscale 3d semantic completion. In *Proceedings of the International Conference on 3D Vision (3DV)*, pages 111–119, 2020. [1](#), [2](#)

[17] Xu Yan, Jiantao Gao, Jie Li, Ruimao Zhang, Zhen Li, Rui Huang, and Shuguang Cui. Sparse single sweep lidar point cloud segmentation via learning contextual shape priors from scene completion. In *Proceedings of the AAAI Conference on Artificial Intelligence (AAAI)*, volume 35, pages 3101–3109, 2021. [1](#), [2](#)

[18] Pengfei Li, Yongliang Shi, Tianyu Liu, Hao Zhao, Guyue Zhou, and Ya-Qin Zhang. Semi-supervised implicit scene completion from sparse lidar. *arXiv preprint arXiv:2111.14798*, 2021. [1](#), [2](#)

[19] Christoph B Rist, David Emmerichs, Markus Enzweiler, and Dariu M Gavrila. Semantic scene completion using local deep implicit functions on lidar data. *IEEE Transactions on Pattern Analysis and Machine Intelligence*, 44(10):7205–7218, 2021. [1](#), [2](#)

[20] Xinhao Liu, Moonjun Gong, Qi Fang, Haoyu Xie, Yiming Li, Hang Zhao, and Chen Feng. Lidar-based 4d occupancy completion and forecasting. *arXiv preprint arXiv:2310.11239*, 2023. [1](#), [3](#)

[21] Zhaoyang Xia, Youquan Liu, Xin Li, Xinge Zhu, Yuexin Ma, Yikang Li, Yuenan Hou, and Yu Qiao. Scpnet: Semantic scene completion on point cloud. In *Proceedings of the IEEE/CVF Conference on Computer Vision and Pattern Recognition*, pages 17642–17651, 2023. [1](#), [3](#)

[22] Tarasha Khurana, Peiyun Hu, David Held, and Deva Ramanan. Point cloud forecasting as a proxy for 4d occupancy forecasting. In *Proceedings of the IEEE/CVF Conference on Computer Vision and Pattern Recognition (CVPR)*, pages 1116–1124, 2023. [1](#), [3](#)

[23] Anh-Quan Cao and Raoul De Charette. Monoscene: Monocular 3d semantic scene completion. In *Proceedings of the IEEE/CVF Conference on Computer Vision and Pattern Recognition (CVPR)*, pages 3991–4001, 2022. [1](#), [2](#), [7](#)

[24] Yuanhui Huang, Wenzhao Zheng, Yunpeng Zhang, Jie Zhou, and Jiwen Lu. Tri-perspective view for vision-based 3d semantic occupancy prediction. In *Proceedings of the IEEE/CVF Conference on Computer Vision and Pattern Recognition (CVPR)*, pages 9223–9232, 2023. [1](#), [3](#)

[25] Yi Wei, Linqing Zhao, Wenzhao Zheng, Zheng Zhu, Jie Zhou, and Jiwen Lu. Surroundocc: Multi-camera 3d occupancy prediction for autonomous driving. In *Proceedings of the IEEE/CVF International Conference on Computer Vision (ICCV)*, pages 21729–21740, 2023. [1](#), [3](#), [7](#), [8](#), [9](#)

[26] Wenwen Tong, Chonghao Sima, Tai Wang, Li Chen, Silei Wu, Hanming Deng, Yi Gu, Lewei Lu, Ping Luo, Dahu Lin, et al. Scene as occupancy. In *Proceedings of the IEEE/CVF International Conference on Computer Vision (ICCV)*, pages 8406–8415, 2023. [1](#), [3](#)

[27] Yunpeng Zhang, Zheng Zhu, and Dalong Du. Occformer: Dual-path transformer for vision-based 3d semantic occupancy prediction. In *Proceedings of the IEEE/CVF International Conference on Computer Vision (ICCV)*, pages 9433–9443, 2023. [1](#), [3](#)

[28] Zhiyu Tan, Zichao Dong, Cheng Zhang, Weikun Zhang, Hang Ji, and Hao Li. Ovo: Open-vocabulary occupancy. *arXiv preprint arXiv:2305.16133*, 2023. [1](#), [3](#)

[29] Yuanhui Huang, Wenzhao Zheng, Borui Zhang, Jie Zhou, and Jiwen Lu. Selfocc: Self-supervised vision-based 3d occupancy prediction. *arXiv preprint arXiv:2311.12754*, 2023. [1](#), [3](#)

[30] Chubin Zhang, Juncheng Yan, Yi Wei, Jiaxin Li, Li Liu, Yansong Tang, Yueqi Duan, and Jiwen Lu. Occnerf: Self-supervised multi-camera occupancy prediction with neural radiance fields. *arXiv preprint arXiv:2312.09243*, 2023. [1](#), [3](#)

[31] Antonin Vobecky, Oriane Siméoni, David Hurich, Spyridon Gidaris, Andrei Bursuc, Patrick Pérez, and Josef Sivic. Pop-3d: Open-vocabulary 3d occupancy prediction from images. *Advances in Neural Information Processing Systems*, 36, 2024. [1](#), [3](#)

[32] Qihang Ma, Xin Tan, Yanyun Qu, Lizhuang Ma, Zhizhong Zhang, and Yuan Xie. Cotr: Compact occupancy transformer for vision-based 3d occupancy prediction. *arXiv preprint arXiv:2312.01919*, 2023. [1](#), [3](#)

[33] Junyi Ma, Xieyuanli Chen, Jiawei Huang, Jingyi Xu, Zhen Luo, Jintao Xu, Weihao Gu, Rui Ai, and Hesheng Wang. Cam4docc: Benchmark for camera-only 4d occupancy forecasting in autonomous driving applications. *arXiv preprint arXiv:2311.17663*, 2023. [1](#), [3](#)

[34] Michael Meyer and Georg Kuschk. Automotive radar dataset for deep learning based 3d object detection. In *Proceedings of the 16th European radar conference (EuRAD)*, pages 129–132. IEEE, 2019. [2](#), [3](#)

[35] Yang Liu, Feng Wang, Naiyan Wang, and ZHAO-XIANG ZHANG. Echoes beyond points: Unleashing the power of raw radar data in multi-modality fusion. *Advances in Neural Information Processing Systems*, 36, 2024. [2](#), [3](#)

[36] Julien Rebut, Arthur Ouaknine, Waqas Malik, and Patrick Pérez. Raw high-definition radar for multi-task learning. In *Proceedings of the IEEE/CVF Conference on Computer Vision and Pattern Recognition (CVPR)*, pages 17021–17030, June 2022. [2](#), [3](#)

[37] Baowei Xu, Xinyu Zhang, Li Wang, Xiaomei Hu, Zhiwei Li, Shuyue Pan, Jun Li, and Yongqiang Deng. Rpfa-net: A 4d radar pillar feature attention network for 3d object detection. In *Proceedings of the IEEE International Intelligent Transportation Systems Conference (ITSC)*, pages 3061–3066. IEEE, 2021. [2](#), [3](#)

[38] Andras Palffy, Ewoud Pool, Srimannarayana Baratam, Julian FP Kooij, and Dariu M Gavrila. Multi-class road user detection with 3+ 1d radar in the view-of-delft dataset. *IEEE Robotics and Automation Letters*, 7(2):4961–4968, 2022. [2](#), [3](#)

[39] Bin Tan, Zhixiong Ma, Xichan Zhu, Sen Li, Lianqing Zheng, Sihan Chen, Libo Huang, and Jie Bai. 3d object detection for multi-frame 4d automotive millimeter-wave radar point cloud. *IEEE Sensors Journal*, 2022. [2](#), [3](#)

[40] Dong-Hee Paek, Seung-Hyun Kong, and Kevin Tirta Wijaya. K-radar: 4d radar object detection for autonomous driving in various weather conditions. *Advances in Neural Information Processing Systems*, 35:3819–3829, 2022. [2](#), [3](#), [4](#), [5](#), [6](#), [7](#), [8](#)

[41] Michael Meyer and Georg Kuschk. Deep learning based 3d object detection for automotive radar and camera. In *Proceedings of the 16th European Radar Conference (EuRAD)*, pages 133–136. IEEE, 2019. [2](#), [3](#)

[42] Li Wang, Xinyu Zhang, Baowei Xv, Jinzhao Zhang, Rong Fu, Xiaoyu Wang, Lei Zhu, Haibing Ren, Pingping Lu, Jun Li, et al. Interfusion: Interaction-based 4d radar and lidar fusion for 3d object detection. In *Proceedings of the IEEE/RSJ International Conference on Intelligent Robots and Systems (IROS)*, pages 12247–12253. IEEE, 2022. [2](#), [3](#)

[43] Li Wang, Xinyu Zhang, Jun Li, Baowei Xv, Rong Fu, Haifeng Chen, Lei Yang, Dafeng Jin, and Lijun Zhao. Multi-modal and multi-scale fusion 3d object detection of 4d radar and lidar for autonomous driving. *IEEE Transactions on Vehicular Technology*, 2022. [2](#), [3](#)

[44] Dong-Hee Paek, Seung-Hyun Kong, and Kevin Tirta Wijaya. Enhanced k-radar: Optimal density reduction to improve detection performance and accessibility of 4d radar tensor-based object detection. In *Proceedings of the IEEE Intelligent Vehicles Symposium (IV)*, pages 1–6. IEEE, 2023. [2](#), [3](#), [4](#), [5](#), [6](#), [7](#), [8](#)

[45] Lianqing Zheng, Zhixiong Ma, Xichan Zhu, Bin Tan, Sen Li, Kai Long, Weiqi Sun, Sihan Chen, Lu Zhang, Mengyue Wan, et al. Tj4dradset: A 4d radar dataset for autonomous driving. In *Proceedings of the IEEE 25th International Conference on Intelligent Transportation Systems (ITSC)*, pages 493–498. IEEE, 2022. [2](#), [3](#)

[46] Jianan Liu, Qiuchi Zhao, Weiyi Xiong, Tao Huang, Qing-Long Han, and Bing Zhu. Smurf: Spatial multi-representation fusion for 3d object detection with 4d imaging radar. *IEEE Transactions on Intelligent Vehicles*, 2023. [2](#), [3](#)

[47] Lianqing Zheng, Sen Li, Bin Tan, Long Yang, Sihan Chen, Libo Huang, Jie Bai, Xichan Zhu, and Zhixiong Ma. Rcfusion: Fusing 4d radar and camera with bird’s-eye view features for 3d object detection. *IEEE Transactions on Instrumentation and Measurement*, 2023. [2](#), [3](#)

[48] Weiyi Xiong, Jianan Liu, Tao Huang, Qing-Long Han, Yuxuan Xia, and Bing Zhu. Lxl: Lidar excluded lean 3d object detection with 4d imaging radar and camera fusion. *IEEE Transactions on Intelligent Vehicles*, 2023. [2](#), [3](#)

[49] Haoyi Zhang, Kai Wu, Rongkang Chen, Zihao Wu, Yong Zhong, and Weihua Li. Tl-4drclf: A two-level 4d radar-camera fusion method for object detection in adverse weather. *IEEE Sensors Journal*, 2024. [2](#), [3](#)

[50] Seung-Hyun Kong, Dong-Hee Paek, and Sangjae Cho. Rtnh+: Enhanced 4d radar object detection network using combined cfar-based two-level preprocessing and vertical encoding. *arXiv preprint arXiv:2310.17659*, 2023. [2](#), [3](#), [4](#)

[51] Qiao Yan and Yihan Wang. Mvfan: Multi-view feature assisted network for 4d radar object detection. In *Proceedings of the International Conference on Neural Information Processing*, pages 493–511. Springer, 2023. [2](#), [3](#)

[52] Xinyu Zhang, Li Wang, Jian Chen, Cheng Fang, Lei Yang, Ziying Song, Guangqi Yang, Yichen Wang, Xiaofei Zhang, and Jun Li. Dual radar: A multi-modal dataset with dual 4d radar for autonomous driving. *arXiv preprint arXiv:2310.07602*, 2023. [2](#), [3](#)

[53] Jianning Deng, Gabriel Chan, Hantao Zhong, and Chris Xiaoxuan Lu. See beyond seeing: Robust 3d object detection from point clouds via cross-modal hallucination. *arXiv preprint arXiv:2309.17336*, 2023. [2](#), [3](#)

[54] Hang Cui, Junzhe Wu, Jiaming Zhang, Girish Chowdhary, and William R Norris. 3d detection and tracking for on-road vehicles with a monovision camera and dual low-cost 4d mmwave radars. In *Proceedings of the IEEE International Intelligent Transportation Systems Conference (ITSC)*, pages 2931–2937. IEEE, 2021. [2](#), [3](#)

[55] Zhijun Pan, Fangqiang Ding, Hantao Zhong, and Chris Xiaoxuan Lu. Moving object detection and tracking with 4d radar point cloud. In *Proceedings of the IEEE International Conference on Robotics and Automation (ICRA)*, 2024. [2](#), [3](#)

[56] Bin Tan, Zhixiong Ma, Xichan Zhu, Sen Li, Lianqing Zheng, Libo Huang, and Jie Bai. Tracking of multiple static and dynamic targets for 4d automotive millimeter-wave radar point cloud in urban environments. *Remote Sensing*, 15(11):2923, 2023. [2](#), [3](#)

[57] Louis L Scharf and Cédric Demeure. *Statistical signal processing: detection, estimation, and time series analysis*. Prentice Hall, 1991. [2](#), [3](#)

[58] Prashant P Gandhi and Saleem A Kassam. Analysis of cfar processors in nonhomogeneous background. *IEEE Transactions on Aerospace and Electronic systems*, 24(4):427–445, 1988. [2](#), [3](#)

[59] Xizhou Zhu, Weijie Su, Lewei Lu, Bin Li, Xiaogang Wang, and Jifeng Dai. Deformable detr: Deformable transformers for end-to-end object detection. In *Proceedings of the International Conference on Learning Representations (ICLR)*, 2020. [2](#), [6](#)

[60] Luis Roldao, Raoul De Charette, and Anne Verroust-Blondet. 3d semantic scene completion: A survey. *International Journal of Computer Vision*, 130(8):1978–2005, 2022. [2](#)

[61] Shuran Song, Fisher Yu, Andy Zeng, Angel X Chang, Manolis Savva, and Thomas Funkhouser. Semantic scene completion from a single depth image. In *Proceedings of the IEEE Conference on Computer Vision and Pattern Recognition (CVPR)*, pages 1746–1754, 2017. [2](#)

[62] Shice Liu, Yu Hu, Yiming Zeng, Qiankun Tang, Beibei Jin, Yinhe Han, and Xiaowei Li. See and think: Disentangling semantic scene completion. *Advances in Neural Information Processing Systems*, 31, 2018. [2](#)

[63] Jiahui Zhang, Hao Zhao, Anbang Yao, Yurong Chen, Li Zhang, and Hongen Liao. Efficient semantic scene completion network with spatial group convolution. In *Proceedings of the European Conference on Computer Vision (ECCV)*, pages 733–749, 2018. [2](#)

[64] Jie Li, Yu Liu, Xia Yuan, Chunxia Zhao, Roland Siegwart, Ian Reid, and Cesar Cadena. Depth based semantic scene completion with position importance aware loss. *IEEE Robotics and Automation Letters*, 5(1):219–226, 2019. [2](#)

[65] Jie Li, Yu Liu, Dong Gong, Qinfeng Shi, Xia Yuan, Chunxia Zhao, and Ian Reid. Rgbd based dimensional decomposition residual network for 3d semantic scene completion. In *Proceedings of the IEEE/CVF Conference on Computer Vision and Pattern Recognition (CVPR)*, pages 7693–7702, 2019. [2](#)

[66] Pingping Zhang, Wei Liu, Yinqie Lei, Huchuan Lu, and Xiaoyun Yang. Cascaded context pyramid for full-resolution 3d semantic scene completion. In *Proceedings of the IEEE/CVF International Conference on Computer Vision (ICCV)*, pages 7801–7810, 2019. [2](#)

[67] Jie Li, Kai Han, Peng Wang, Yu Liu, and Xia Yuan. Anisotropic convolutional networks for 3d semantic scene completion. In *Proceedings of the IEEE/CVF Conference on Computer Vision and Pattern Recognition (CVPR)*, pages 3351–3359, 2020. [2](#)

[68] Xiaokang Chen, Kwan-Yee Lin, Chen Qian, Gang Zeng, and Hongsheng Li. 3d sketch-aware semantic scene completion via semi-supervised structure prior. In *Proceedings of the IEEE/CVF Conference on Computer Vision and Pattern Recognition (CVPR)*, pages 4193–4202, 2020. [2](#)

[69] Yingjie Cai, Xuesong Chen, Chao Zhang, Kwan-Yee Lin, Xiaogang Wang, and Hongsheng Li. Semantic scene completion via integrating instances and scene in-the-loop. In *Proceedings of the IEEE/CVF Conference on Computer Vision and Pattern Recognition (CVPR)*, pages 324–333, 2021. [2](#)

[70] Jens Behley, Martin Garbade, Andres Milioto, Jan Quenzel, Sven Behnke, Cyrill Stachniss, and Jurgen Gall. Semantickitti: A dataset for semantic scene understanding of lidar sequences. In *Proceedings of the IEEE/CVF International Conference on Computer Vision (ICCV)*, pages 9297–9307, 2019. [2](#), [7](#)

[71] Fangqiang Ding, Andras Palfy, Dariu M Gavrila, and Chris Xiaoxuan Lu. Hidden gems: 4d radar scene flow learning using cross-modal supervision. In *Proceedings of the IEEE/CVF Conference on Computer Vision and Pattern Recognition*, pages 9340–9349, 2023. [3](#)

[72] Fangqiang Ding, Zhijun Pan, Yimin Deng, Jianning Deng, and Chris Xiaoxuan Lu. Self-supervised scene flow estimation with 4-d automotive radar. *IEEE Robotics and Automation Letters*, 7(3):8233–8240, 2022. [3](#)

[73] Jun Zhang, Huayang Zhuge, Yiyao Liu, Guohao Peng, Zhenyu Wu, Haoyuan Zhang, Qiyang Lyu, Heshan Li, Chunyang Zhao, Dogan Kircali, et al. Ntu4dradlm: 4d radar-centric multi-modal dataset for localization and mapping. In *Proceedings of the IEEE 26th International Conference on Intelligent Transportation Systems (ITSC)*, pages 4291–4296. IEEE, 2023. [3](#)

[74] Minseong Choi, Seunghoon Yang, Seungho Han, Yeongseok Lee, Minyoung Lee, Keun Ha Choi, and Kyung-Soo Kim. Msc-rad4r: Ros-based automotive dataset with 4d radar. *IEEE Robotics and Automation Letters*, 2023. [3](#)

[75] Shouyi Lu, Guirong Zhuo, Lu Xiong, Xichan Zhu, Lianqing Zheng, Zihang He, Mingyu Zhou, Xinfei Lu, and Jie Bai. Efficient deep-learning 4d automotive radar odometry method. *IEEE Transactions on Intelligent Vehicles*, 2023. [3](#)

[76] Guirong Zhuoins, Shouyi Lu, Lu Xiong, Huanyu Zhouins, Lianqing Zheng, and Mingyu Zhou. 4drvo-net: Deep 4d radar–visual odometry using multi-modal and multi-scale adaptive fusion. *IEEE Transactions on Intelligent Vehicles*, 2023. [3](#)

[77] Yuan Zhuang, Binliang Wang, Jianzhu Huai, and Miao Li. 4d iriom: 4d imaging radar inertial odometry and mapping. *IEEE Robotics and Automation Letters*, 2023. [3](#)

[78] Xingyi Li, Han Zhang, and Weidong Chen. 4d radar-based pose graph slam with ego-velocity pre-integration factor. *IEEE Robotics and Automation Letters*, 2023. [3](#)

[79] Jun Zhang, Huayang Zhuge, Zhenyu Wu, Guohao Peng, Mingxing Wen, Yiyao Liu, and Danwei Wang. 4dradar slam: A 4d imaging radar slam system for large-scale environments based on pose graph optimization. In *Proceedings of the IEEE International Conference on Robotics and Automation (ICRA)*, pages 8333–8340. IEEE, 2023. [3](#)

[80] Julien Rebut, Arthur Ouaknine, Waqas Malik, and Patrick Pérez. Raw high-definition radar for multi-task learning. In *Proceedings of the IEEE/CVF Conference on Computer Vision and Pattern Recognition (CVPR)*, pages 17021–17030, 2022. [3](#)

[81] Guoqiang Zhang, Haopeng Li, and Fabian Wenger. Object detection and 3d estimation via an fmcw radar using a fully convolutional network. In *Proceedings of the IEEE International Conference on Acoustics, Speech and Signal Processing (ICASSP)*, pages 4487–4491. IEEE, 2020. [3](#)

[82] Yizhou Wang, Zhongyu Jiang, Yudong Li, Jenq-Neng Hwang, Guanbin Xing, and Hui Liu. Rodnet: A real-time radar object detection network cross-supervised by camera-radar fused object 3d localization. *IEEE Journal of Selected Topics in Signal Processing*, 15(4):954–967, 2021. [3](#)

[83] Xu Dong, Pengluo Wang, Pengyue Zhang, and Langechuan Liu. Probabilistic oriented object detection in automotive radar. In *Proceedings of the IEEE/CVF Conference on Computer Vision and Pattern Recognition Workshops (CVPRW)*, pages 102–103, 2020. 3

[84] Ao Zhang, Farzan Erlik Nowruzi, and Robert Laganiere. Raddet: Range-azimuth-doppler based radar object detection for dynamic road users. In *Proceedings of the 18th Conference on Robots and Vision (CRV)*, pages 95–102. IEEE, 2021. 3

[85] Andras Palfy, Jiaao Dong, Julian FP Kooij, and Dariu M Gavrila. Cnn based road user detection using the 3d radar cube. *IEEE Robotics and Automation Letters*, 5(2):1263–1270, 2020. 3

[86] Bence Major, Daniel Fontijne, Amin Ansari, Ravi Teja Sukhavasi, Radhika Gowaikar, Michael Hamilton, Sean Lee, Slawomir Grzechnik, and Sundar Subramanian. Vehicle detection with automotive radar using deep learning on range-azimuth-doppler tensors. In *Proceedings of the IEEE/CVF International Conference on Computer Vision Workshops (ICCVW)*, 2019. 3

[87] Texas Instruments. mmWave Radar Sensors - Overview. <https://www.ti.com/sensors/mmwave-radar/overview.html>, 2024. Accessed: 2024-02-22. 3

[88] Andrew Kramer, Kyle Harlow, Christopher Williams, and Christoffer Heckman. Coloradar: The direct 3d millimeter wave radar dataset. *The International Journal of Robotics Research*, 41(4):351–360, 2022. 3

[89] Stephen Blake. Os-cfar theory for multiple targets and nonuniform clutter. *IEEE Transactions on Aerospace and Electronic Systems*, 24(6):785–790, 1988. 3

[90] Yuwei Cheng, Jingran Su, Mengxin Jiang, and Yimin Liu. A novel radar point cloud generation method for robot environment perception. *IEEE Transactions on Robotics*, 38(6):3754–3773, 2022. 3

[91] Du Tran, Lubomir Bourdev, Rob Fergus, Lorenzo Torresani, and Manohar Paluri. Learning spatiotemporal features with 3d convolutional networks. In *Proceedings of the IEEE International Conference on Computer Vision (ICCV)*, pages 4489–4497, 2015. 5, 6

[92] Yin Zhou and Oncel Tuzel. Voxelnet: End-to-end learning for point cloud based 3d object detection. In *Proceedings of the IEEE Conference on Computer Vision and Pattern Recognition (CVPR)*, pages 4490–4499, 2018. 5, 6

[93] R Kwok and C Haas. Effects of radar side-lobes on snow depth retrievals from operation icebridge. *Journal of Glaciology*, 61(227):576–584, 2015. 5

[94] Peter Tait. *Introduction to radar target recognition*, volume 18. IET, 2005. 5

[95] Ming Nie, Yujing Xue, Chunwei Wang, Chaoqiang Ye, Hang Xu, Xinge Zhu, Qingqiu Huang, Michael Bi Mi, Xinchao Wang, and Li Zhang. Partner: Level up the polar representation for lidar 3d object detection. In *Proceedings of the IEEE/CVF International Conference on Computer Vision (ICCV)*, pages 3801–3813, 2023. 5

[96] Xinge Zhu, Hui Zhou, Tai Wang, Fangzhou Hong, Yuexin Ma, Wei Li, Hongsheng Li, and Dahua Lin. Cylindrical and asymmetrical 3d convolution networks for lidar segmentation. In *Proceedings of the IEEE/CVF Conference on Computer Vision and Pattern Recognition (CVPR)*, pages 9939–9948, 2021. 5

[97] Ashish Vaswani, Noam Shazeer, Niki Parmar, Jakob Uszkoreit, Llion Jones, Aidan N Gomez, Łukasz Kaiser, and Illia Polosukhin. Attention is all you need. *Advances in neural information processing systems*, 30, 2017. 5

[98] Yan Yan, Yuxing Mao, and Bo Li. Second: Sparsely embedded convolutional detection. *Sensors*, 18(10):3337, 2018. 6

[99] Kaiming He, Xiangyu Zhang, Shaoqing Ren, and Jian Sun. Deep residual learning for image recognition. In *Proceedings of the IEEE Conference on Computer Vision and Pattern Recognition (CVPR)*, pages 770–778, 2016. 6

[100] Tsung-Yi Lin, Piotr Dollár, Ross Girshick, Kaiming He, Bharath Hariharan, and Serge Belongie. Feature pyramid networks for object detection. In *Proceedings of the IEEE Conference on Computer Vision and Pattern Recognition (CVPR)*, pages 2117–2125, 2017. 7

- [101] Maxim Berman, Amal Rannen Triki, and Matthew B Blaschko. The lovász-softmax loss: A tractable surrogate for the optimization of the intersection-over-union measure in neural networks. In *Proceedings of the IEEE Conference on Computer Vision and Pattern Recognition (CVPR)*, pages 4413–4421, 2018. [7](#)
- [102] Yiming Li, Sihang Li, Xinhao Liu, Moonjun Gong, Kenan Li, Nuo Chen, Zijun Wang, Zhiheng Li, Tao Jiang, Fisher Yu, et al. Sscbench: A large-scale 3d semantic scene completion benchmark for autonomous driving. *arXiv preprint arXiv:2306.09001*, 2023. [7](#)